

# Brain tumor detection through image fusion using whale optimization and edge preserving filter

Bhattiprolu Nagasirisha<sup>1,\*</sup> , Venkatesh Munagala<sup>2</sup> , Ramakrishna Reddy Eamani<sup>3</sup> , Mocherla Venkata Srikanth<sup>3</sup> , Asileti Suneel Kumar<sup>3</sup> , Varre Venkata Kanaka Durga Vara Prasad<sup>1</sup> 

<sup>1</sup>Gudlavalleru Engineering College, Andhra Pradesh, India.

<sup>2</sup>Vasireddy Venkataadri Institute of Technology, Andhra Pradesh, India.

<sup>3</sup>Usha Rama College of Engineering and Technology, Andhra Pradesh, India.

<sup>4</sup>Gudlavalleru Engineering College, Andhra Pradesh, India.

\*Corresponding author: [nagasirishab@gmail.com](mailto:nagasirishab@gmail.com)

## Original Research

Received:

30 August 2024

Revised:

26 December 2024

Accepted:

8 January 2025

Published online:

1 March 2025

© 2025 The Author(s). Published by the OICC Press under the terms of the [Creative Commons Attribution License](https://creativecommons.org/licenses/by/4.0/), which permits use, distribution and reproduction in any medium, provided the original work is properly cited.

## Abstract:

In diagnostic imaging, image fusion remains a significant difficulty, particularly in medical applications like guided image operations and radiation therapy. By maintaining the pertinent details and characteristics of the original images, medical image fusion aims to increase the precision of disease diagnosis. This study suggests a novel methodology for MRI and CT image fusion that uses the proposed tri-scale decomposition with Gaussian and guided filters to decompose the source images into base and detail layers. Each source image is guided through guided filtering using Gaussian curvature as guidance. While the detail layers are fused based on maximum energy assessed using the Krisch compass operator, the base layers are fused based on the whale optimization method, for which the objective function is maximization of entropy, edge strength and pixel intensity. Thirty different kinds of slices of five medical datasets from diverse sources were used to assess the effectiveness of the proposed algorithm both visually and statistically compared to existing approaches. Based on both objective evaluation and qualitative image analysis, the experimental results demonstrated that the suggested strategy performed better than other widely used techniques. In comparison to the existing methods under consideration, the quantitative results show that the proposed algorithm improves the standard deviation by 16%, mutual information by 41%, spatial frequency by 12%, image entropy by 6.5%, edge strength of the fused image by 37%, and structural similarity index by 31%.

**Keywords:** Image fusion; Gaussian; Guided filter; Whale optimization; Krisch compass; Entropy; Edge strength and pixel intensity

## 1. Introduction

Numerous sensors can now capture a wide range of images because of the quick development of sensor technologies. Magnetic Resonance Imaging (MRI), Positron Emission Tomography (PET), Computed Tomography (CT), Single Photon Emission Computed Tomography (SPECT), Green Fluorescent Protein (GFP), and Phase Contrast (PC) imaging are among the methods frequently used in multimodal biomedical imaging. A 3D depiction of lesions and accurate localization are made possible by MRI's thorough cross-sectional, sagittal, coronal, and inclined-plane views of the human body. Higher-density tissues, such as bone, are represented as brighter areas on CT scans, which show how various organs and tissues absorb X-rays. Because of this, CT scans are useful for locating the dense tissues of body.

Different amounts of tracer molecules that are injected into the circulation and correlate to different degrees of tissue activity are detected by radiation-based imaging techniques like PET and SPECT. Because of this, PET and SPECT are especially helpful in locating and detecting aberrant metabolic activity in tissues, which helps detect diseases. GFP and PC are two often used imaging techniques in molecular biology. PC imaging is useful for identifying minute alterations in cellular constituents such as the mitochondria, cytoplasm, or nucleus because it provides insight into the structural characteristics of cells. In contrast, the distribution of proteins can be seen by GFP imaging. GFP images emphasize the dispersion of proteins, but PC images provide superior grayscale spatial resolution. Combining these benefits is the aim of PC-GFP image fusion, which preserves the phase contrast structural characteristics of an

image while enabling the detection of areas with strong protein activity. By offering more precise protein localization and in-depth information, this fusion improves biomedical analysis. But only one kind of image can be captured by a single sensor. By merging images from many modalities, image fusion creates a composite image with better visual quality and more detailed information. Image fusion is therefore a very useful tool in many domains, such as object identification, computer-aided diagnostics, and image retrieval and classification.

Although there are many different fusion approaches, the majority of them use multiscale and multi-resolution transformation (MST-MRT) methods. Multiscale characteristics can be captured using MST-MRT-based algorithms at a variety of resolutions, and the fusion results can be enhanced by applying different fusion rules to different layers. Non-Subsampled Shearlet Transform (NSST) [1, 2], Non-Subsampled Contourlet Transform (NSCT) [3, 4], wavelet-based techniques [5, 6], and pyramid-based approaches [7, 8] are some of the MST-based methods that have been developed. With flexible fusion strategies for wavelet coefficients, wavelet-based fusion methods use the wavelet transform to extract multi-scale features. The fused image is then produced by applying the inverse wavelet transform. Despite providing flexible decomposition using different wavelet basis functions, wavelet-based fusion techniques often result in fuzzy fused images due to the considerable amount of detail lost throughout the process.

The decomposition and fusing processes of pyramid-based fusion approaches also result in the loss of detail. A more recent and faster class of transformations is NSST and NSCT, which provide multi-scale and multi-directional transformations. Although high-frequency coefficient loss during the fusion process can still lead to fuzzy edges and blurred features, these techniques can help fused images retain their edges and details to some degree. Sparse representation (SR) [9], which is another popular fusion technique, is made up of two primary parts: dictionary learning and coefficient optimization. SR is quite flexible and can be used for restoration, information fusion, and image denoising. SR-based fusion algorithms do have certain limitations, though. It can be difficult to choose the right dictionary size, for instance a dictionary that is too big slows down the fusion process, whereas a dictionary that is too tiny yields incomplete information and less than ideal fusion results. Furthermore, it can be challenging to select the best optimization technique because different approaches yield varied fusion outcomes. The speed and effective filtering capabilities of filter-based algorithms have made them prominent in imaging. A significant breakthrough was made in 2013 with the introduction of guided image filters [10]. However, because it solely takes spatial weights into account, its capacity to maintain edges and minimize noise is constrained. To overcome these constraints, the rolling guidance filter [11] was put forth in 2014; it takes into account both range and spatial weights and incorporates numerous guidance processes. Consequently, the rolling guidance filter can remove small details while maintaining large-scale structures. Deep convolutional neural networks (CNNs)

[12, 13] have been popular in imaging-related applications in recent years. Convolution, pooling, and activation layers are the three primary layers that make up CNNs. CNNs can fit a wide range of data once they have been taught. Because of their adaptability, they can be used for a variety of challenging tasks, such as image fusion, classification, segmentation, and super-resolution.

Recent years have seen the development of numerous meta-heuristic optimization strategies that have been effectively used to medical image fusion. Some noteworthy examples include Quantum-behaved Particle Swarm Optimization (QPSO) [14], Modified Central Force Optimization (MCFO) [15], Gray Wolf Optimization [16], Chaotic Grey Wolf Optimization (CGWO) [17], Hybrid Genetic and Grey Wolf Optimization (HG-GWO) [18], Particle Swarm Optimization with Non-Subsampled Shearlet Transform (NSST-PSO) [19], Binary Crow Search Optimization (BCSO) [20], Modified Shark Smell Optimization (MSSO) [21], and Cartoon-texture decomposition utilizing Particle Swarm Optimization (TV-PSO) based on Total Variation (TV) [22]. Recent developments in medical image fusion and brain tumor segmentation offer a context for assessing the novelty of this work. Multi-level edge fusion is integrated into Sparse Dynamic Volume TransUNet for brain tumor segmentation, whereas Lightweight Medical Image Segmentation Networks employ multi-scale feature-guided fusion [23–27]. Nevertheless, rather than enhancing the fused image quality directly, these works mostly concentrate on segmentation. By improving both the base and detail layers, our approach, on the other hand, addresses the fusion quality and allows for more accurate diagnostic interpretations.

There are several problems with the current image fusion techniques. The low-frequency component fusion approach, which applies a weighted average rule, is the first limitation. The brightness intensity of the combined image is reduced as a result of this limitation. The second disadvantage is the poor fusing of high-frequency coefficients. Current techniques struggle to preserve specific information because their preservation indices are too low. Important information in the fused image may be lost as a result. This work is motivated by the pressing need for better fusion techniques that maintain contrast and diagnostic information. For instance, perfect fusion helps define regions of interest and detect small anomalies, which are essential in applications such as surgical planning and tumor detection.

In this paper, we propose a novel approach that employs two algorithms to address these limitations. The key advantages of the recommended approach are outlined below:

1. The Whale Optimization approach (WOA) is utilized to determine the optimal parameters for fusing base layers in order to ensure that the fused image has improved contrast.
2. The Kirsch compass mask, which effectively preserves the detailed information of the input images in the fused image, is employed to give an efficient fusion rule of the detail layers.

## 2. Background

### 2.1 Guided image filter

Guided filter is used to produce base layers that are smooth and noise-free. The filter suppresses noise and improves edge preservation by using Gaussian curvature as guidance. Both large-scale and small-scale detail layers are obtained by subtracting the output at different points in time. The definition of the output  $F$  at a pixel ‘ $i$ ’ for a guided image  $P$  centered at pixel ‘ $k$ ’ within a square window  $w_k$  is given by equation (1)

$$F_i = m_k P_i + n_k, \forall_i \in w_k \tag{1}$$

In this case, the linear coefficients  $m_k$  and  $n_k$  are found within the window  $w_k$  by minimizing the subsequent cost function.

$$E(m_k, n_k) = \sum_{i \in w_k} ((m_k P_i + n_k - I_i)^2 + \epsilon m_k^2) \tag{2}$$

The regularization parameter in this equation is  $\epsilon$ . The ideal values that minimize the objective function for  $m_k$  and  $n_k$  are determined as follows:

$$m_k = \frac{\frac{1}{|w|} \sum_{i \in w_k} P_i I_i - \mu_k E[I_k]}{\sigma_k^2 + \epsilon} \tag{3}$$

$$n_k = E[I_k] - m_k \mu_k \tag{4}$$

In this case, the total number of pixels in  $w_k$ , is represented by  $|w|$ . The mean and variance of the window  $w_k$  are represented by  $\mu_k$ , and  $\sigma_k^2$ ; the expected value of  $I$  in  $w_k$  is indicated by  $E[I_k]$ . Equation (1) is used to calculate the filtered output,  $F_i$ , after the coefficients  $m_k$  and  $n_k$  have been determined.

Because overlapping windows share pixels, all overlapping estimates of  $F_i$  are averaged to provide the final output.

$$F_i = \bar{m}_i P_i + \bar{n}_i \tag{5}$$

Section 2.2.1 describes the equations and parameters, including a regularization term of 0.01 and a neighborhood size of 15.

### 2.2 Tri-scale image decomposition

There are numerous algorithms for splitting an image into multi scales. These algorithms have been used to various medical image fusion methodologies. In this study, we introduced the tri-scale image decomposition method. Figure 1 shows the proposed picture decomposition method. Here, the base layer, which comprises homogenous portions of the image, is created by applying a Gaussian filter to the input image. The detail layers are extracted by applying the source image to a guided filter, which uses the guidance image as the Gaussian curvature of the source image. The output of the Gaussian filter is subtracted from the output of the guided filter to obtain the detail layer with large variations, and the output of the guided filter is subtracted from the original image to obtain the detail layer with tiny scale changes. Targeted processing is made possible by tri-scale decomposition, which clearly separates base layers (uniform regions) from detail layers (fine features). In contrast to conventional two-scale techniques, this method minimizes noise interference and preserves more fine features. Because of the extra filtering processes, the tri-scale decomposition is computationally demanding even though it is successful.

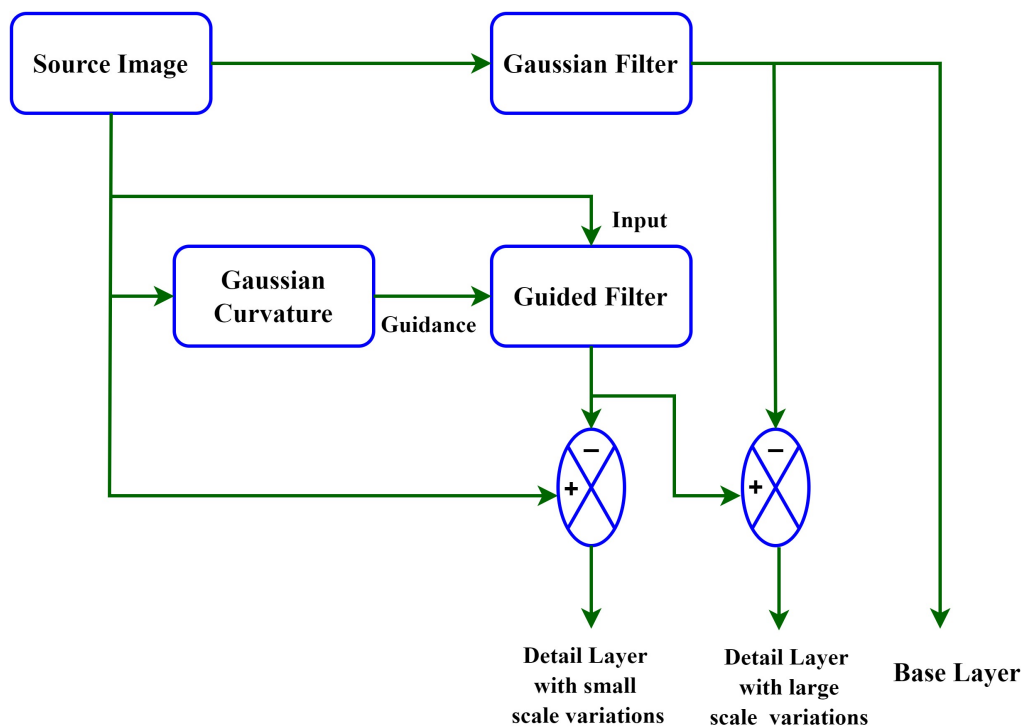


Figure 1. Proposed Tri-scale image decomposition model.

### 2.2.1 Algorithm of proposed tri-scale decomposition

Step 1: Let the input image to be decomposed is  $I_1$

Step 2: Base layer of  $I_1$  is obtained is filtering it using Gaussian lowpass filter with  $\sigma = 3$ .

$$I_B = \text{Gaussian}(I_1, 3) \quad (6)$$

where Gaussian function of 2D is defined as  $I_1(x, y, \sigma) = \frac{1}{2\pi\sigma^2} \exp(-\frac{x^2+y^2}{2\sigma^2})$ , with  $(x, y)$  representing the spatial coordinates of an image.

Step 3: Obtain the Gaussian curvature of input image as follows:

Obtain the smoothed image of  $I_1$  using equation (7)

$$I_s = \text{Gaussian}(I_1, 3) \quad (7)$$

Compute the first order partial derivatives of  $I_s$  along  $x$  and  $y$  directions to get gradient.

$$I_x = \frac{\partial I_s}{\partial x} \quad \text{and} \quad I_y = \frac{\partial I_s}{\partial y} \quad (8)$$

Compute the second order partial derivatives of  $I_s$  along  $x$  and  $y$  directions

$$I_{xx} = \frac{\partial^2 I_s}{\partial x^2} \quad \text{and} \quad I_{yy} = \frac{\partial^2 I_s}{\partial y^2} \quad \text{and} \quad I_{xy} = \frac{\partial^2 I_s}{\partial x \partial y} \quad (9)$$

Compute Gaussian curvature ( $K$ ) of an image using the following relation

$$K = \frac{I_{xx}I_{yy} - I_{xy}^2}{(1 + I_x^2 + I_y^2)^2} \quad (10)$$

The denominator  $(1 + I_x^2 + I_y^2)^2$  ensures that the curvature is scaled appropriately based on the gradients of the image.

Through the integration of data from an image's maximum and minimum curvatures, Gaussian curvature offers a thorough assessment of surface variance. This makes it especially well-suited for capturing and maintaining subtle transitions and details, which are essential in medical imaging. In medical images, mean curvature tends to emphasize smoother transitions and could miss structural details or sharp edges. As a scalar approximation of curvature, the Laplacian is less accurate in distinguishing between concave and convex regions, which could result in the loss of important information. Experimental results demonstrate the higher edge and detail retention of the suggested strategy, which reflects the balanced approach that Gaussian curvature offers by combining comprehensiveness and precision.

Step 4: Obtain the Guided filtered image ( $I_G$ ) of input image by taking Gaussian curvature ( $K$ ) as guidance image.

$$I_G = \text{guided filter}(I_1, K, r, \epsilon) \quad (11)$$

where  $r, \epsilon$  are the size of neighborhood and regularization parameters of guided filter which are taken as 15 and 0.01.

Step 5: Compute the detail layer with small scale variations ( $I_{DS}$ ) by subtracting the guided filtered image from original image.

$$I_{DS} = I_1 - I_G \quad (12)$$

Step 6: Compute the detail layer with large scale variations ( $I_{DL}$ ) by subtracting the Gaussian filtered image from guided filtered image.

$$I_{DL} = I_G - I_B \quad (13)$$

The results of proposed novel tri-scale image decomposition technique are illustrated in figure 2. Equations (6), (12) and (13) are used to produce base, detail layer with small scale

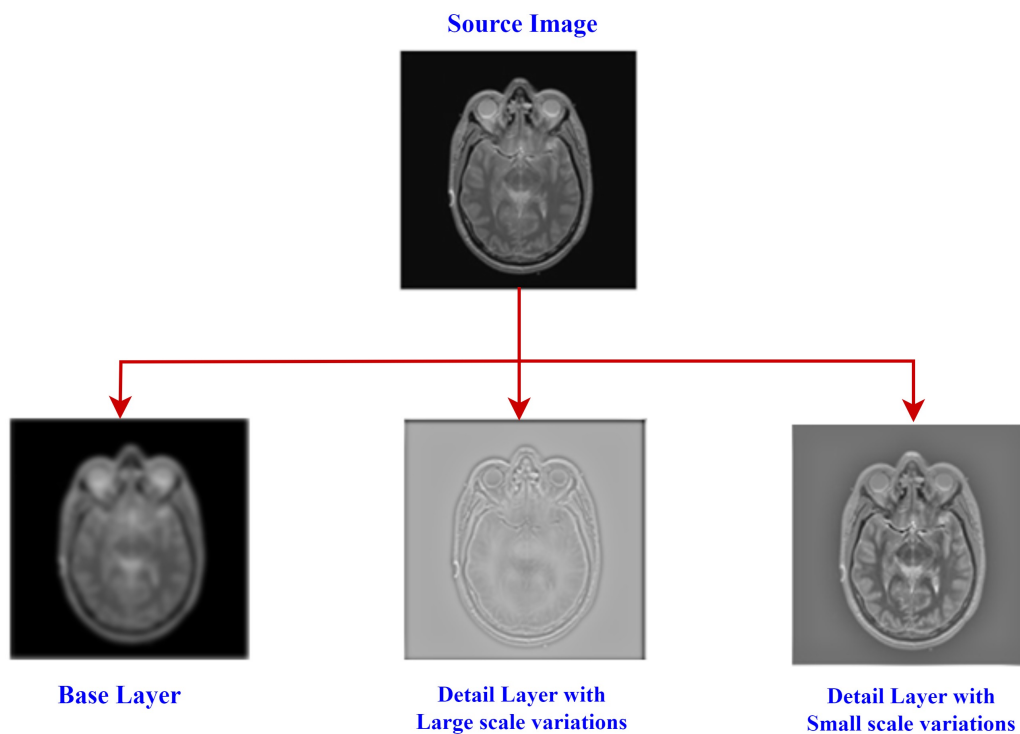


**Figure 2.** An example of proposed tri-scale image decomposition.

variations ( $I_{DS}$ ), detail layer with large scale variations ( $I_{DL}$ ) using tri-scale decomposition.

**2.3 Whale optimization algorithm**

The Whale Optimization Algorithm (WOA) is inspired by the hunting behavior of humpback whales, particularly their bubble-net feeding strategy [22]. This algorithm is used for solving optimization problems, including image thresholding. It mainly contain following steps:

**2.4 Initialization**

Start by randomly generating  $n$  whales within the search space. Each whale represents a potential solution, i.e., a set of threshold values for image segmentation. Let the  $i^{th}$  individual in the population is given as  $X_i = [X_{i1}, X_{i2} \dots X_{id}]$  (where  $d$  is the dimensionality of problem which means number of unknowns to be calculated). Each population is initialized using equation (14).

$$X_i = LB + rand(UB - LB) \text{ where } i = 1 \text{ to } n \quad (14)$$

where  $LB$  - lower bound of image intensity, which is taken as 0 and  $UB$  - upper bound of image intensity, which is taken as 255.  $rand$  is a random number in the interval [0,1]

**2.5 Encircling prey (exploitation)**

Let  $X_i$  be the position of  $i^{th}$  whale in the population. Then the position update formula is given as follows:

$$X_i(t + 1) = X^*(t) - \vec{A} * \vec{D} \quad (15)$$

$$\vec{D} = |\vec{C} * X^*(t) - X_i(t)| \quad (16)$$

where  $\vec{C}$  and  $\vec{A}$  are coefficient vectors,  $t$  is the current iteration number and  $t + 1$  is the next iteration number.

$$\vec{A} = 2a * \vec{r}_1 - a \quad (17)$$

$$\vec{C} = 2\vec{r}_2 \quad (18)$$

$\vec{r}_1$  and  $\vec{r}_2$  are the random vectors in the interval [0,1] and ‘ $a$ ’ is the convergence factor. The value of ‘ $a$ ’ decreases linearly from 2 to 0 as the number of iterations increases, the formula for calculating ‘ $a$ ’ is given as  $a = 2 - \frac{2t}{T}$  (where ‘ $T$ ’ is the maximum number of iteration)

**2.5.1 Bubble-net attacking method (exploration)**

The bubble net attack mimics how whales hunt and catch prey by employing spiral bubble nets. Equation (19) provides an updated formula for the bubble net attack’s location.

$$X_i(t + 1) = \vec{D}' * e^{bl} * \cos(2\pi l) + X_{best}(t) \quad (19)$$

where  $b$  is the constant used to define the shape of the logarithmic spiral,  $l$  is the random number between [-1,1].

**2.5.2 Random search stage**

Whales not only use bubble nets for foraging, but they also conduct haphazard searches for food. Every whale updates its position in relation to other random whales during the random search phase, hence broadening the search area.

Equation (20) is used to express the location of the random search stage.

$$X_i(t + 1) = X_r(t) - \vec{A} * \vec{D} \quad (20)$$

$$\vec{D} = |\vec{C} * X_r(t) - X_i(t)| \quad (21)$$

The suggested image fusion approach in the research relies heavily on the Whale Optimization Algorithm (WOA) to fuse the base layers of the source images. The primary objective is to find the best fusion settings to improve image quality, which optimizes the fusion process. The purpose of WOA is to maximize a specified objective function that incorporates important metrics like entropy, edge strength and contrast so that fused image guarantees the high information richness and maintains edge and structural components of the original images by preserving pixel intensity.

**3. Proposed fusion approach**

In this section, we suggest two novel algorithms. The first one is suggested to combine detail layers and is based on the Kirsch compass operator. The second algorithm uses the tri-scale image decomposition method and the Whale Optimization Algorithm to combine medical images.

**3.1 Kirsch compass operator based fusion rule**

A sharp image has significantly more energy in its detail layers than one that is blurry. Details layers hold the fine details of an image. As a result, certain methods, such as the NSCT transform with local energy and the empirical wavelet decomposition with maximum local energy utilized fusion rule based on maximum local energy. Our proposal for a new fusion rule for detail layers is driven by the efficiency of the local energy function and is based on the Kirsch operator. One technique for locating the edge is the compass operator. There are several popular compass operators, including the Robinson, Prewitt, Kirsch, and isotropic compass operators. Among them, the Kirsch operator has proven to be the most effective of these compass operators. Russell Kirsch originally presented the Kirsch operator in 1971. North (N), North-West (NW), West (W), South-West (SW), South (S), South-East (SE), East (E), and North-East (NE) are the eight directions in which this approach employs eight kernel masks as shown in figure 3.

We proposed a new fusion rule for fusing the detail layers based on maximum energy computed using Kirsch operator.

**3.1.1 Algorithm for fusing the detail layers**

Step 1: Take detail layers of two source images obtained from tri-scale image decomposition as inputs. Let they are labeled as  $I_{D1}$  and  $I_{D2}$ .

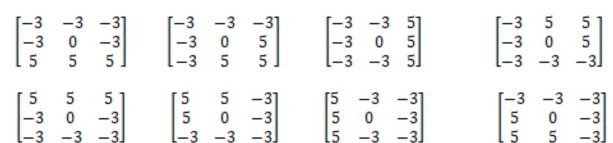


Figure 3. Illustration of Kirsch masks in eight directions.

Step 2: Compute the energy of detail each layer in eight directions ( $E_1$  to  $E_8$ ) by applying Kirsch masks.

$$E_K(x,y) = \sum_{t_1=-1}^1 \sum_{t_2=-1}^1 M_K(t_1,t_2) * I_D^2(x-t_1,y-t_2) \quad (22)$$

for  $K = 1$  to 8

where  $M_K$  is the Kirsch mask in  $K^{\text{th}}$  direction.

Step 3: Compute maximum energy layer from the eight available energy layers by pixel by pixel comparison.

$$E_{\max}(x,y) = \max(E_i(x,y)) \quad \text{where } i = 1 \text{ to } 8 \quad (23)$$

Using steps 2 and 3, compute the maximum energy layers of detail layers of two source images by replacing  $I_D^2$  with  $I_{D1}^2$  and  $I_{D2}^2$ , which are labeled as  $E_{\max}^1$  and  $E_{\max}^2$

Step 4: Fuse the detail layers winner-takes first rule as follows:

$$\begin{aligned} I_{DF}(x,y) &= I_{D1}(x,y) \text{ if } E_{\max}^1(x,y) \geq E_{\max}^2(x,y) \\ &= I_{D2}(x,y) \text{ if } E_{\max}^1(x,y) < E_{\max}^2(x,y) \end{aligned} \quad (24)$$

Energy computed on detail layers using Kirsch compass operator in eight directions along with maximum energy layer is depicted in figure 4. The function of the Kirsch Compass Operator for detail fusion is to calculate edge information in eight directional masks. In the fused image, it reduces redundant information and highlights fine features by choosing the direction with the highest energy. The Sobel operator, on the other hand, is computationally effective and appropriate for edge detection; however, it mainly concentrates on horizontal and vertical gradients, potentially leading to the loss of diagonal edge characteristics. Similar to this, the Canny edge detector is more computationally complex and requires several processing steps (such as Gaussian smoothing, gradient estimation, non-maximum suppression, and thresholding), even though it is quite precise at identifying edges with less noise. Furthermore, weaker but

clinically relevant edges found in medical pictures may be unintentionally excluded by Canny's thresholding procedure.

### 3.2 Proposed algorithm based on Tri-scale decomposition and WOA

The proposed approach of image fusion is illustrated in figure 5 and it contain following steps:

Step 1: Read Input images  $I_1$  and  $I_2$  that needs to be fused

Step 2: Apply proposed tri-scale decomposition mechanism and decompose the input images into coarse layers ( $I_{B1}$  and  $I_{B2}$ ), detail layers with significant variations ( $I_{DL1}$  and  $I_{DL2}$ ) and detail layers with small scale variations ( $I_{DS1}$  and  $I_{DS2}$ ).

Step 3: Fuse the detail layers using proposed fusion rule based on Kirsch compass operator ( $FR-KCO$ ) energy.

$$D_a = FR - KCO(I_{DS1}, I_{DS2}) \quad (25)$$

$$D_b = FR - KCO(I_{DL1}, I_{DL2}) \quad (26)$$

Step 4: The base layer fusion is performed using a linear combination of two base layers, controlled by the fusion parameter  $\beta \in [0,1]$  which will be optimized.

$$\text{Fused base layer, } I_{Bf} = \beta * I_{B1} + (1 - \beta) * I_{B2} \quad (27)$$

Step 5: Combining the fused based layer and the fused detail layers yields the final fused image.

$$\text{Fused Image, } I_{\text{fused}} = I_{Bf} + D_a + D_b \quad (28)$$

Step 6: Objective function ( $OF$ ) is modeled as weighted sum of edge strength, entropy and mean pixel intensity and is used as maximization problem.

$$OF = \beta_1 * E_{\text{edge}}(I_{\text{fused}}) + \beta_2 * H(I_{\text{fused}}) + \beta_3 * M(I_{\text{fused}}) \quad (29)$$

where  $E_{\text{edge}}(I_{\text{fused}})$  indicates the edge strength of fused image and is calculated using the Laplacian filter. It is defined

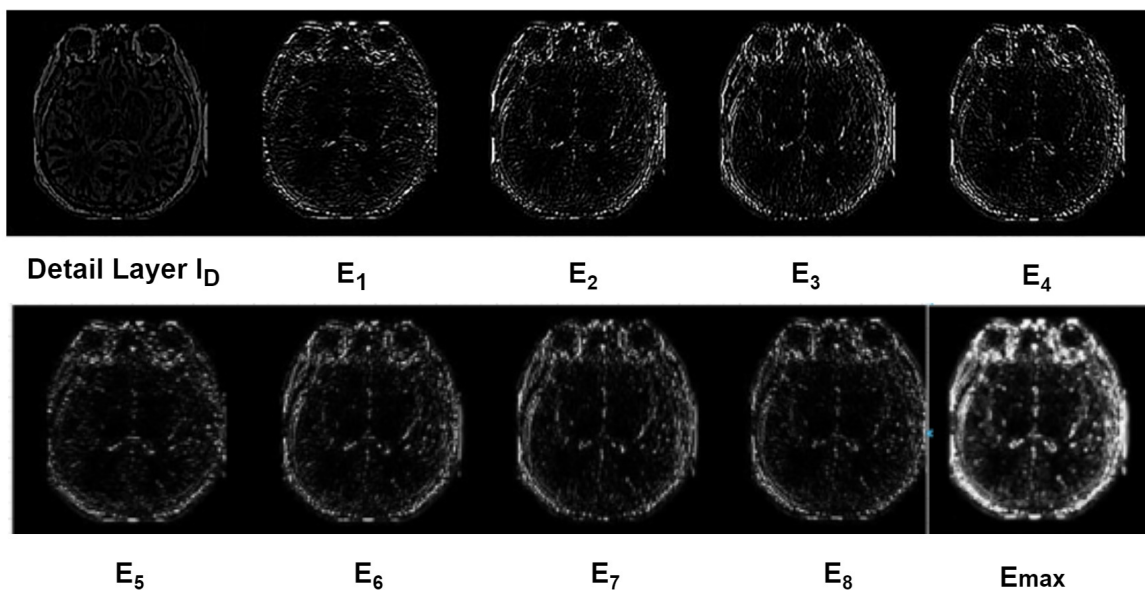


Figure 4. Illustration of energy layers computed using KCO on detail layer.

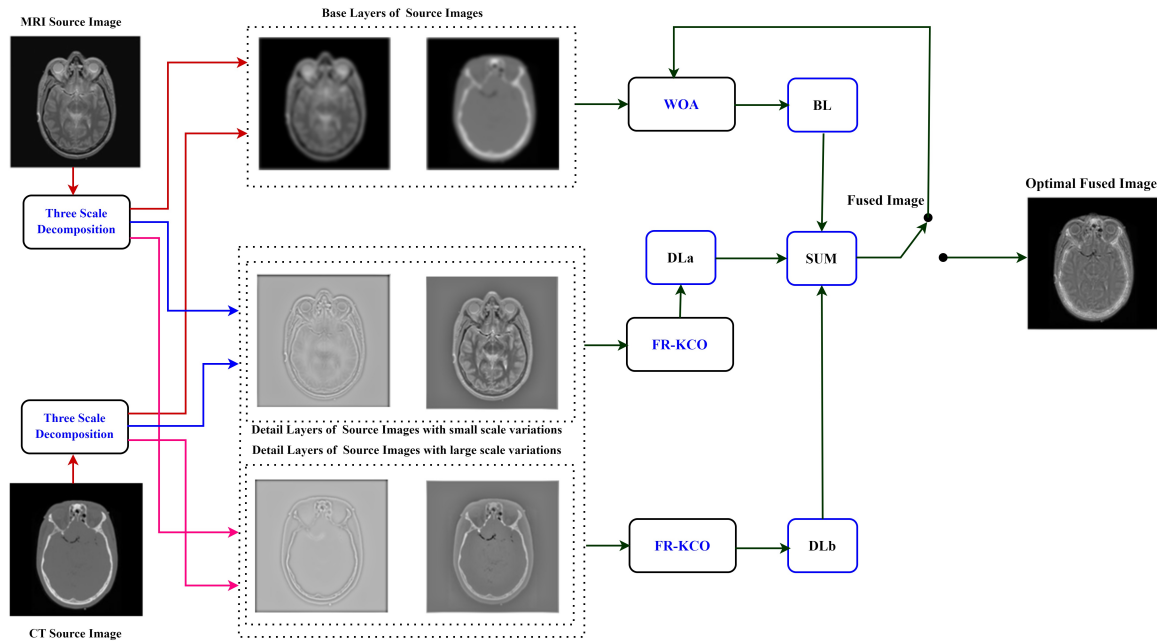


Figure 5. Proposed mechanism of image fusion.

as the accumulation of the absolute values of the Laplacian-filtered image.

$$E_{edge}(I_{fused}) = \sum_i \sum_j |L(I_{fused}(i, j))| \quad (30)$$

where  $(i, j)$ -coordinates of pixels of an image  $H(I_{fused})$  indicates entropy, which measures information content in an image. For an image with probability of pixel intensity distribution  $P_k$ ,  $H(I_{fused})$  can be calculated using equation (31).

$$H(I_{fused}) = - \sum_{k=0}^{255} P_k \log(P_k) \quad (31)$$

$M(I_{fused})$  indicates the Mean value of all pixel intensities in the fused image. For a  $256 \times 256$  image,  $M = 256$  and  $N = 256$  and  $M(I_{fused})$  is computed using equation (32).

$$M(I_{fused}) = \frac{1}{MN} \sum_{i=1}^M \sum_{j=1}^N I_{fused}(i, j) \quad (32)$$

$\beta_1$ ,  $\beta_2$  and  $\beta_3$  are the weighting factors of edge strength, entropy and mean pixel intensity of fused image. Choosing appropriate values for the weights  $\beta_1$ ,  $\beta_2$  and  $\beta_3$  in the objective function depends on the specific requirements and characteristics of the image fusion task. If the primary goal is to preserve the sharpness, structural details, and boundaries (e.g., in medical or satellite images), edge strength should be prioritized. In this case,  $\beta_1$  is assigned higher value. If the objective is to maximize information content or contrast (e.g., for high-contrast imaging tasks), then entropy should have more influence. Increasing  $\beta_2$  will help emphasize contrast and fine details. To have an image with more brightness,  $\beta_3$  is assigned more value. A sensitivity study was conducted on the objective function's weighting parameters. 0.5 (edge strength), 0.3 (entropy), and 0.2 (mean

intensity) were shown to be the ideal weights, guaranteeing robustness across different datasets. Hence In our work, values of  $\beta_1$ ,  $\beta_2$  and  $\beta_3$  are taken as 0.5, 0.3, 0.2 respectively. Step 7: The objective function is used to guide the WOA in finding the optimal fusion parameter ( $\beta$ ), ensuring the maximization of edge strength, entropy, and mean pixel intensity.

$$\beta_{optimal} = \arg \max(OF(\beta)) \quad (33)$$

Step 8: Using the  $\beta_{optimal}$ , Fused base layer relation of equation (27) is modified as follows:

$$I_{Bf_{optimal}} = \beta_{optimal} * I_{B1} + (1 - \beta_{optimal}) * I_{B2} \quad (34)$$

Step 9: From the optimal fused base layer, Optimal fused image is obtained using equation (35).

$$I_{fused_{optimal}} = I_{Bf_{optimal}} + D_a + D_b \quad (35)$$

## 4. Results and discussion

### 4.1 Subjective analysis

The proposed method was implemented and evaluated using an Intel Core i3 CPU running at 2.4 GHz with 8 GB of RAM and Windows 10 64-bit operating system. We made use of MATLAB 2020a, which has built-in toolboxes for image processing, optimization, and programming. Five MRI and CT scan datasets related to brain diseases, designated "Dataset-I" through "Dataset-V," are selected to evaluate the effectiveness of the proposed image fusion method. Sagittal perspective images of the brain and skull (Dataset-IV), a brain with cerebellar metastases (Dataset-V), a patient's brain bleeding to death (Dataset-II), a brain with neoplastic cancer (Dataset-III), and a healthy brain (Dataset-I) are all included in these datasets [28]. Each image has 256 by 256 pixels and is made up of 256 grayscale levels. The datasets are sourced from [29] and are available at [http://www.med.harvard.edu/aanlib/home.html], the

website for the Benchmark Brain Atlas. The fusion results for Dataset-I are shown in figure 6, where CT and MRI source images are shown in Figs. 6(a) and (b). The results of several fusion strategies, such as Sparse Representation (SR), Discrete Wavelet Transform (DWT), Non-Subsampled Shearlet Transform (NSST), Convolutional Neural Network (CNN), guided filter approach and the proposed method are displayed from figs. 6(c) through (h). There are slight variations in how detail and contrast are maintained between the modalities, despite the fact that the connective tissue details acquired by MRI and the skeletal structure from CT are typically conserved. A yellow rectangle draws attention to the differences between the different fusion procedures. The emphasized region of the fused pictures, as seen in Figs. 6(c) and (d), exhibits a rather weak brightness.

Certain information from the MRI scan is usually lost, even though the CT image information is usually retained in the NSST and CNN methods as observed in Figs. 6(e) and (f). The visual clarity of the guided filter is comparable to our proposed method that can preserve all the features of the original image. As seen in Figs. 6(g)-(h), the intensity of the guided filter technique is lower than that of our approach. The second set of medical images is called Dataset-II, and the fusion results are displayed in Fig. 7. The application of DWT leaves hard tissues containing bone structures, with minimal information and visual impact, as seen in Fig. 7(d). Fig. 7(c) similarly illustrates this low intensity problem. The

outcomes of the remaining three currently used approaches did not differ substantially. Since our approach is unable to discern between the intensity fluctuations of pixels in the CT scan on a row-by-row and column-by-column basis, in contrast to the guided filter, the CT information is not as well retained in this situation. The proposed methodology produced a fused image with great contrast and full retention of soft tissue information, as illustrated in Fig. 8(h), which compares the suggested method with alternative comparison techniques using a third clinical data set (Dataset-III). Figures 9 and 10 display the fusion results of Datasets IV and V, where the SR, DWT and NSST methods provide insufficient information on the bone structure and lose details of the original images. The recommended method produces results with more contrast, sharper edges, and finer details. To assess fusion performance, both qualitative and quantitative evaluation criteria must be used. This research uses quantitative assessment measures, including Standard Deviation (SD), Mutual Information (MI), Image Entropy (H), Spatial Frequency (SF), Mean Structural Similarity Index Measure (MSSIM), and Edge Strength ( $Q_{AB/F}$ ), to evaluate the efficacy of several fusion procedures [30]. The quantitative assessments employing image evaluation metrics are summarized in Table 2. Mathematical formulation of these metrics are presented in Table 1. The best outcomes are presented in bold. The proposed methodology for fusing image data performed much better in terms of MI, H,  $Q_{AB/F}$ , and MSSIM, while the other metrics are hardly

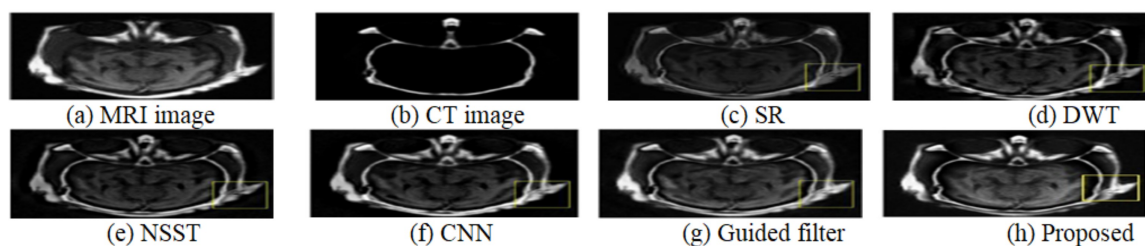


**Figure 6.** Fusion results of Dataset-I (CT-MRI of healthy brain).

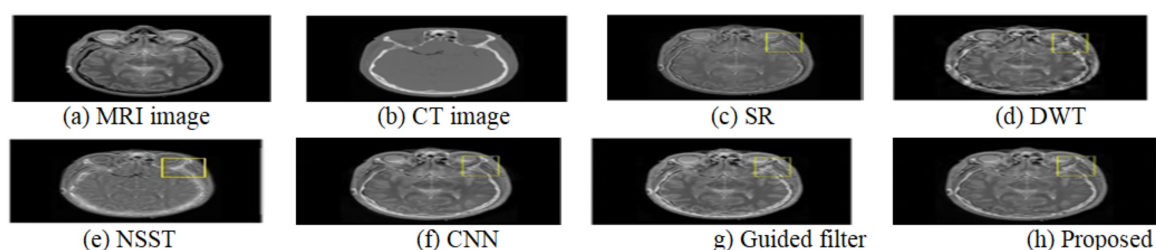


**Figure 7.** Fusion results of Dataset-II (CT-MRI of Fatal stroke).

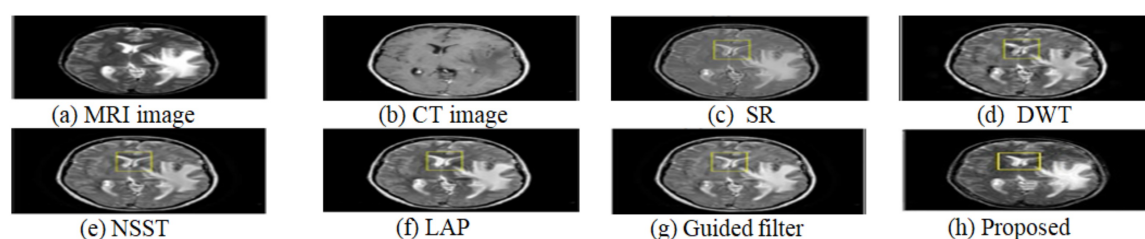


**Figure 8.** Fusion results of Dataset-III (CT-MRI of neoplastic tumor).

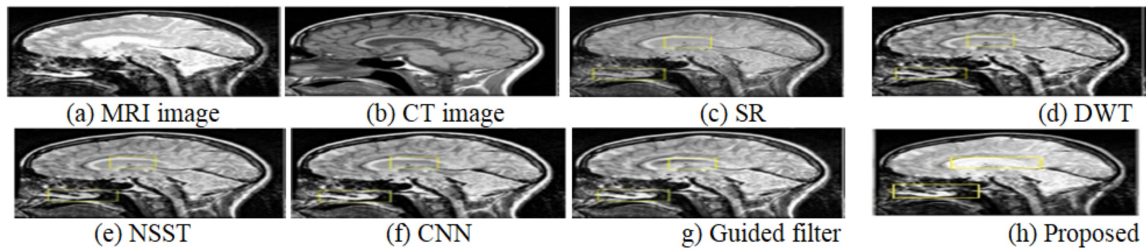


Figure 9. Fusion results of Dataset-IV (CT-MRI of brain skull).

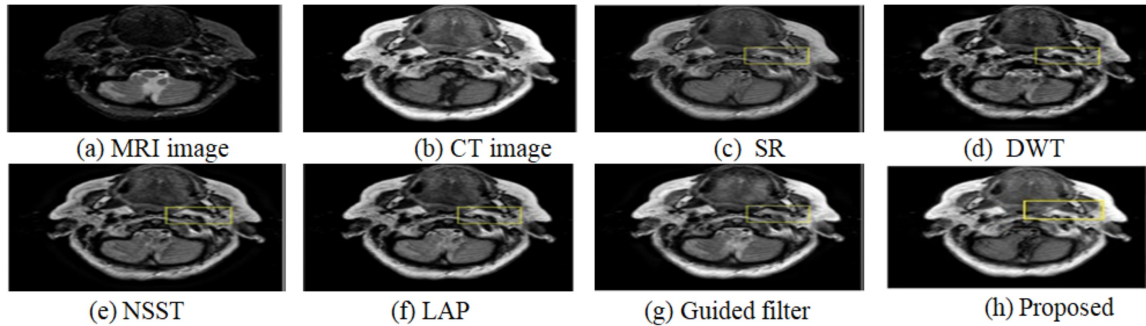


Figure 10. Fusion results of Dataset-V (CT-MRI of Cerebella metastasis).

Table 1. Advantages and disadvantages of GFM converter control methodologies.

Performance Metric	Mathematical formulae
Average Pixel Intensity (API)	For an image $f(i, j)$ of size $M \times N$ , $API = \frac{1}{MN} \sum_{i=1}^M \sum_{j=1}^N f(i, j)$ Higher value of API produces an image with more contrast.
Standard Deviation (SD)	It is a metric for the level of deviation in a mean collection of image data. $SD = \sqrt{\frac{1}{MN} \sum_{i=1}^M \sum_{j=1}^N (f(i, j) - API)^2}$
Image Entropy (H)	It estimates information content in an image. Large value of H indicates an image with more information. For an image with probability of pixel intensity distribution $P_k$ , entropy is calculated as follows: $H = -\sum_{k=0}^{255} P_k \log(P_k)$
Mutual Information (MI)	For two source images $A, B$ and fused image $F$ , Mutual information is given as $MI_F^{AB} = MI(A, F) + MI(B, F)$ $MI(A, F) = \sum_{z \in Z} \sum_{y \in Y} p(A, F) \log_2 \frac{p(A, F)}{p(A)p(F)}$ $MI(B, F) = \sum_{z \in Z} \sum_{y \in Y} p(B, F) \log_2 \frac{p(B, F)}{p(B)p(F)}$ The quantity of activity level data that is transmitted from the source images into the fused image is measured.
Spatial Frequency (SF)	It measures an resolution level of an image. Higher value is desired. $SF(i, j) = \sqrt{ RF(i, j) ^2 +  CF(i, j) ^2}$ $RF(i, j) = \sqrt{\frac{1}{M \times N} \sum_{i=2}^M \sum_{j=2}^N [I(i, j) - I(i, j-1)]^2}$ $CF(i, j) = \sqrt{\frac{1}{M \times N} \sum_{i=2}^M \sum_{j=2}^N [I(i, j) - I(i-1, j)]^2}$
Edge Strength (( $Q_{AB/F}$ ))	$Q_{AB/F}$ represents the degree to which the edge information from the input images transitions into the fused image. The evaluation is as follows: $Q_{AB/F} = \frac{\sum_{i=1}^M \sum_{j=1}^N (Q_{AF}(i, j)W_A(i, j) + Q_{BF}(i, j)W_B(i, j))}{\sum_{i=1}^M \sum_{j=1}^N (W_A(i, j) + W_B(i, j))}$
Mean Structural Similarity Index Measure (MSSIM)	$SSIM(A, F) = \frac{(2\mu_A\mu_F + C_1)(2\sigma_{AF} + C_2)}{(\mu_A^2 + \mu_F^2 + C_1)(\sigma_A^2 + \sigma_F^2 + C_2)}$ The variance of A is represented by $\sigma_A^2$ , the variance of F by $\sigma_F^2$ , the covariance of A and F by $\sigma_{AF}$ , and the mean of A and F by $\mu_A$ and $\mu_F$ , respectively. The usage of two constants, $C_1$ and $C_2$ , prevents the instability that can arise from a division with a value close to zero. SSIM readings are a number between 0 and 1, where 1 denotes exceptional quality and 0 denotes poor quality. Less distortion is present in the fused image when the MSSIM score is greater. $MSSIM = \frac{SSIM(A, F) + SSIM(B, F)}{2}$

**Table 2.** Statistical parameters of proposed approach for multimodal datasets.

Dataset type	Method	Standard Deviation (SD)	Mutual Information (MI)	Spatial Frequency (SF)	Image Entropy (H)	Edge Strength (QAB/F)	MSSIM
Dataset-I	SR	30.82	2.57	11.68	5.80	0.5756	0.5122
	DWT	44.71	1.92	17.13	6.17	0.6073	0.5246
	NSST	44.16	2.05	17.05	6.20	0.6816	0.5366
	CNN	52.89	2.43	17.40	6.07	0.7184	0.5518
	Guided filter (GF)	52.89	2.31	16.97	6.52	0.7210	0.5634
	Proposed	<b>57.22</b>	<b>5.63</b>	<b>20.21</b>	<b>6.73</b>	<b>0.8207</b>	<b>0.9938</b>
Dataset-II	SR	51.40	3.42	17.76	4.94	0.5178	0.8248
	DWT	55.73	3.19	22.01	5.19	0.5051	0.7915
	NSST	54.56	3.34	20.95	5.12	0.5887	0.8160
	CNN	59.92	3.34	21.93	4.89	0.5888	0.8146
	Guided filter (GF)	55.68	3.79	20.25	5.20	0.6028	0.8207
	Proposed	<b>62.50</b>	<b>3.99</b>	<b>24.58</b>	<b>4.86</b>	<b>0.8040</b>	<b>0.9940</b>
Dataset-III	SR	61.50	3.18	20.19	4.52	0.5157	0.7640
	DWT	66.53	3.12	25.11	4.86	0.5473	0.7489
	NSST	65.89	3.20	24.52	4.88	0.5971	0.7733
	CNN	69.60	3.38	25.99	4.39	0.6042	0.7775
	Guided filter (GF)	69.63	3.34	24.39	5.05	0.6119	0.7762
	Proposed	<b>72.81</b>	<b>4.39</b>	<b>26.38</b>	<b>5.17</b>	<b>0.8009</b>	<b>0.9831</b>
Dataset-IV	SR	69.84	3.33	28.98	7.56	0.4964	0.6532
	DWT	76.80	3.08	35.94	7.41	0.4699	0.6263
	NSST	79.49	3.23	34.60	7.44	0.5349	0.6628
	CNN	79.84	3.26	32.85	7.31	0.5171	0.6462
	Guided filter (GF)	75.36	3.52	34.30	7.60	0.5510	0.6602
	Proposed	<b>85.97</b>	<b>5.22</b>	<b>37.03</b>	<b>7.76</b>	<b>0.8250</b>	<b>0.9847</b>
Dataset-V	SR	51.71	3.19	17.58	5.24	0.4823	0.7427
	DWT	55.72	2.80	22.28	5.36	0.4573	0.7098
	NSST	53.79	2.94	21.47	5.44	0.5226	0.7311
	CNN	61.11	3.18	23.06	4.83	0.5214	0.7448
	Guided filter (GF)	66.98	3.23	21.56	5.60	0.5330	0.7342
	Proposed	<b>74.64</b>	<b>4.63</b>	<b>25.98</b>	<b>5.78</b>	<b>0.8625</b>	<b>0.9899</b>

comparable, suggesting that it can maintain saliency data and edge features. Figure 11 depicts a visual comparison of numerous methodologies based on the average values of four essential relevant assessment metrics (MI, H, MSSIM, and  $Q_{AB/F}$ ) measured over thirty datasets.

### 4.2 Result analysis

The experimental findings show that the Sparse Representation (SR) and DWT techniques perform poorly in fusion when there is little intensity and insufficient bone structure information. While NSST, guided filter and CNN approaches have a noticeable visual impact, they does not

completely retain the edge and texture of the yellow highlighted zone. Furthermore, the Guided Filter technique failed to sustain color in the MR-SPECT & MR-PET fusion circumstances. However, the proposed method preserves saliency traits, which provide the most information about soft tissue and bone anatomy, resulting in crisper and more colorful fused images. Standard deviation (SD), Image entropy (H) and spatial frequency (SF) are three of the six metrics taken into consideration. These metrics are widely used to evaluate the quality of fused images and show the intrinsic characteristics of a single image. The entropy represents the fused image’s data entropy. The image is rendered

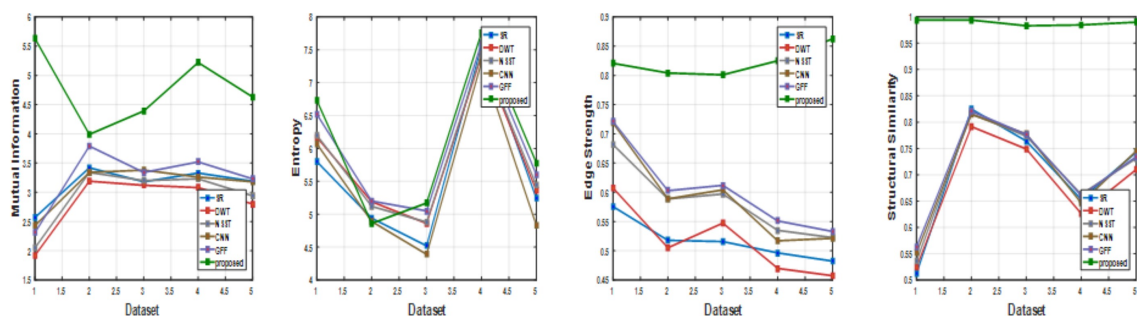


**Figure 11.** Comparative analysis of average values of quality evaluation metrics.

clear by the SF. The combined image's contrast is described by the SD. While a higher contrast makes it easier to perceive the fused image, a larger SD causes the image's grey level dispersion to be more widely spread. Some existing techniques include duplicate elements, which increase the value for each of these metrics. This work introduces three new measures to allow for a more full objective examination:  $Q_{AB/F}$ , MI and SSIM. The MI measures the similarity of the intensity distributions of the connected image pairs while also estimating the amount of information extracted from the source images. The MI value grows as more data is transferred from the original images, as well as the clarity and activity level of the combined image. The MSSIM determines the level of distortion in the composite image.  $Q_{AB/F}$  additionally evaluates the amount of edge information transferred from the primary images to the fused image. With the addition of more edge information, such as texture & bone structure, this parameter becomes more important for clinical image fusion. This is because it allows for accurate clinical assessment of edges. A statistical analysis of results of both existing as well as proposed techniques revealed that the proposed mechanism enhances standard deviation by 16%, mutual information by 41%, spatial frequency by 12%, image entropy by 6.5%, edge details of the fused image by 37% and structural similarity index by 31%, when compared to existing methods. This demonstrates that the fused image was minimally distorted and contained an acceptable amount of soft tissue details, prominent features, bone structures, and important edge details.

## 5. Conclusion

The proposed study addresses shortcomings in current fusion algorithms by introducing a novel approach to MRI and CT image fusion that successfully blends tri-scale image decomposition, the Whale Optimization Algorithm (WOA), and the Krisch compass operator. The technique assures effective fusion and maintains important features by breaking down source images into basic and detail layers. In order to provide superior edge preservation and feature retention, the WOA maximizes entropy, edge strength, and pixel intensity while fusing the base layer. At the same time, an energy maximization method based on the Krisch compass operator is employed to fuse the detail layers. Numerous tests showed that the suggested approach produces fused images with sharper edges, higher contrast, and improved representation of soft tissue and bone structures, outperforming current methods in terms of quality assessment metrics. This work could be expanded in the future by adding more modalities, integrating deep learning for parameter optimization, creating real-time clinical applications, creating adaptive objective functions for particular diagnostic tasks, and investigating novel evaluation metrics that are more in line with clinical requirements, like boundary sharpness and lesion detectability. With these improvements, the usefulness of suggested framework and adaptability may be further increased, expanding its potential for patient care and clinical diagnostics.

### Authors contributions

Authors have contributed equally in preparing and writing the manuscript.

### Availability of data and materials

The data that support the findings of this study are available from the corresponding author upon reasonable request.

### Conflict of interests

The authors declare that they have no known competing financial interests or personal relationships that could have appeared to influence the work reported in this paper.

## References

- [1] X. Liu, W. Mei, and H. Du. "Multi-modality medical image fusion based on image decomposition framework and nonsubsampling shearlet transform." *Biomed. Signal Process. Control*, 40:343–350, 2018.  
DOI: <https://doi.org/10.1016/j.bspc.2017.10.001>.
- [2] Z. Ding, D. Zhou, R. Nie, R. Hou, and Y. Liu. "Brain medical image fusion based on dual branch CNNs in NSST domain." *BioMed Res. Int.*, 2020:1–15, 2020.  
DOI: <https://doi.org/10.1155/2020/6265708>.
- [3] Z. Zhu, M. Zheng, G. Qi, D. Wang, and Y. Xiang. "A phase congruency and local Laplacian energy based multi-modality medical image fusion method in NSCT domain." *IEEE Access*, 7:20811–20824, 2019.  
DOI: <https://doi.org/10.1109/access.2019.2898111>.
- [4] S. Wang and Y. Shen. "Multi-modal image fusion based on saliency guided in NSCT domain." *IET Image Process*, 2020.  
DOI: <https://doi.org/10.1049/iet-ipr.2019.1319>.
- [5] Y. Yang. "A novel DWT based multi-focus image fusion method." *Proc. Eng.*, 24:177–181, 2011.  
DOI: <https://doi.org/10.1016/j.proeng.2011.11.2622>.
- [6] B. Yu, B. Jia, L. Ding, Z. Cai, Q. Wu, R. Law, J. Huang, L. Song, and S. Fu. "Hybrid dual tree complex wavelet transform and support vector machine for digital multi-focus image fusion." *Neurocomputing*, 182:1–9, 2016.  
DOI: <https://doi.org/10.1016/j.neucom.2015.10.084>.
- [7] J. Du, W. Li, B. Xiao, and Q. Nawaz. "Union Laplacian pyramid with multiple features for medical image fusion." *Neurocomputing*, 194:326–339, 2016.  
DOI: <https://doi.org/10.1016/j.neucom.2016.02.047>.
- [8] J. Fu, W. Li, J. Du, and B. Xiao. "Multimodal medical image fusion via Laplacian pyramid and convolutional neural network reconstruction with local gradient energy strategy." *Comput. Biol. Med.*, 126:104048, 2020.  
DOI: <https://doi.org/10.1016/j.combiomed.2020.104048>.
- [9] Y. Liu, X. Chen, R. K. Ward, and Z. J. Wang. "Image fusion with convolutional sparse representation." *IEEE Signal Process. Lett.*, 23(12):1882–1886, 2016.  
DOI: <https://doi.org/10.1109/lsp.2016.2618776>.
- [10] S. Li, X. Kang, and J. Hu. "Image Fusion With Guided Filtering." *IEEE Transactions on Image Processing*, 22(7):2864–2875, 2013.  
DOI: <https://doi.org/10.1109/TIP.2013.2244222>.
- [11] Q. Zhang, X. Shen, L. Xu, and J. Jia. "Rolling Guidance Filter." *Springer, Cham.*, 8691, 2014.  
DOI: <https://doi.org/10.1007/978-3-319-10578-9-53>.
- [12] W. Tan, J. Zhang, P. Xiang, H. Zhou, and W. Thiton. "Infrared and visible image fusion via NSST and PCNN in multiscale morphological gradient domain." *Optics, Photonics and Digital Technologies for Imaging Applications VI, SPIE*, 2020.  
DOI: <https://doi.org/10.1117/12.2551830>.

- [13] M. Yin, X. Liu, Y. Liu, and X. Chen. "Medical Image Fusion With Parameter-Adaptive Pulse Coupled Neural Network in Nonsampled Shearlet Transform Domain." *IEEE Transactions on Instrumentation and Measurement*, 64(1):49–64, 2019. DOI: <https://doi.org/10.1109/TIM.2018.2838778>.
- [14] X. Xu, D. Shan, G. Wang, and X. Jiang. "Multimodal medical image fusion using PCNN optimized by the QPSO algorithm." *Applied Soft Computing*, 46:588–595, 2016. ISSN 1568-4946. DOI: <https://doi.org/10.1016/j.asoc.2016.03.028>.
- [15] M. H. El-Hoseny, W. Abd El-Rahman, M. El-Sayed El-Rabaie, E. Fathi Abd El-Samie, and S. Osama Faragallah. "An efficient DT-CWT medical image fusion system based on modified central force optimization and histogram matching." *Infrared Physics & Technology*, 94:223–231, 2018. ISSN 1350-4495. DOI: <https://doi.org/10.1016/j.infrared.2018.09.003>.
- [16] E. Daniel, J. Anitha, K. K. Kamaleshwaran, and I. Rani. "Optimum spectrum mask based medical image fusion using Gray Wolf Optimization." *Biomedical Signal Processing and Control*, 34:36–43, 2017. ISSN 1746-8094. DOI: <https://doi.org/10.1016/j.bspc.2017.01.003>.
- [17] C. S. Asha, S. Lal, V. P. Gurupur, and P. U. P. Saxena. "Multi-Modal Medical Image Fusion With Adaptive Weighted Combination of NSSB Bands Using Chaotic Grey Wolf Optimization." *IEEE Access*, 7:40782–40796, 2019. DOI: <https://doi.org/10.1109/ACCESS.2019.2908076>.
- [18] E. Daniel. "Optimum Wavelet-Based Homomorphic Medical Image Fusion Using Hybrid Genetic–Grey Wolf Optimization Algorithm." *IEEE Sensors Journal*, 18(16):6804–6811, 2018. DOI: <https://doi.org/10.1109/JSEN.2018.2822712>.
- [19] V. S. Parvathy and S. Pothiraj. "Multi-modality medical image fusion using hybridization of binary crow search optimization." *Health Care Manag Sci*, 23:661–669, 2020. DOI: <https://doi.org/10.1007/s10729-019-09492-2>.
- [20] K. Padmavathi, C. S. Asha, and V. Karki Maya. "A novel medical image fusion by combining TV-L1 decomposed textures based on adaptive weighting scheme." *Engineering Science and Technology, an International Journal*, 23(1):225–239, 2020. ISSN 2215-0986. DOI: <https://doi.org/10.1016/j.jestch.2019.03.00>.
- [21] A. Tannaz, S. Mousa, D. Sabalan, et al. "Fusion of multimodal medical images using nonsubsampling shearlet transform and particle swarm optimization." *Multidim Syst Sign Process*, 31:269–287, 2020. DOI: <https://doi.org/10.1007/s11045-019-00662-7>.
- [22] S. Mirjalili and A. Lewis. "The whale optimization algorithm." *Adv. Eng. Softw.*, 95:51–67, 2016. DOI: <https://doi.org/10.1016/j.advengsoft.2016.01.008>.
- [23] Z. Zhu, M. Sun, G. Qi, Y. Li, X. Gao, and Y. Liu. "Sparse Dynamic Volume TransUNet with multi-level edge fusion for brain tumor segmentation." *Computers in Biology and Medicine*, 172:108284, 2024. DOI: <https://doi.org/10.1016/j.combiomed.2024.108284>.
- [24] Z. Zhu, K. Yu, G. Qi, B. Cong, Y. Li, Z. Li, and X. Gao. "Lightweight medical image segmentation network with multi-scale feature-guided fusion." *Computers in Biology and Medicine*, 182:109204, 2024. DOI: <https://doi.org/10.1016/j.combiomed.2024.109204>.
- [25] Z. Zhu, Z. Wang, G. Qi, N. Mazur, P. Yang, and Y. Liu. "Brain tumor segmentation in MRI with multi-modality spatial information enhancement and boundary shape correction." *Pattern Recognition*, 153:110553, 2024. DOI: <https://doi.org/10.1016/j.patcog.2024.110553>.
- [26] X. Shen, J. Wang, Y. Zhao, R. Zhou, H. Gao, J. Zhang, and H. Shen. "MRS-Net: Brain tumour segmentation network based on feature fusion and attention mechanism." *IET Image Processing*, 18(14):4542–4550, 2024. DOI: <https://doi.org/10.1049/ipr2.13266>.
- [27] Z. Zhu, X. He, G. Qi, Y. Li, B. Cong, and Y. Liu. "Brain tumor segmentation based on the fusion of deep semantics and edge information in multimodal MRI." *Information Fusion*, 91:376–387, 2023. DOI: <https://doi.org/10.1016/j.inffus.2022.10.022>.
- [28] M. Venkata Srikanth, A. Suneel Kumar, B. Nagasirisha, and T. Lakshmi. "Brain MRI and CT Image Fusion Using Multiscale Local Extrema and Image Statistics." *ECTI-EEC*, 22(1), 2024. DOI: <https://doi.org/https://doi.org/10.37936/ecti-ee.2024221.249146>.
- [29] K. A. Johnson and J. Alex Becker. "The whole brain atlas." 2012. URL <https://www.med.harvard.edu/aanlib/>.
- [30] S. M. V. S. Kethavath, S. Yerram, S. Kalli, B. Nagasirisha, and J. Brahmaiah Naik. "Brain Tumor Detection through Image Fusion Using Cross Guided Filter and Convolutional Neural Network." *ECTI-CIT Transactions*, 18(4):579–590, 2024. DOI: <https://doi.org/10.37936/ecti-cit.2024184.256650>.